NANOMEDICINE

Clinical translation of an ultrasmall inorganic optical-PET imaging nanoparticle probe

Evan Phillips,[1] Oula Penate-Medina,[1]* Pat B. Zanzonico,[2] Richard D. Carvajal,[3] Pauliah Mohan,[1] Yunpeng Ye,[1] John Humm,[2] Mithat Gönen,[4] Hovanes Kalaigian,[2] Heiko Schöder,[1] H. William Strauss,[1] Steven M. Larson,[1] Ulrich Wiesner,[5] Michelle S. Bradbury[1†]

A first-in-human clinical trial of ultrasmall inorganic hybrid nanoparticles, "C dots" (Cornell dots), in patients with metastatic melanoma is described for the imaging of cancer. These renally excreted silica particles were labeled with ^{124}I for positron emission tomography (PET) imaging and modified with cRGDY peptides for molecular targeting. ^{124}I-cRGDY–PEG–C dot particles are inherently fluorescent, containing the dye, Cy5, so they may be used as hybrid PET-optical imaging agents for lesion detection, cancer staging, and treatment management in humans. However, the clinical translation of nanoparticle probes, including quantum dots, has not kept pace with the accelerated growth in minimally invasive surgical tools that rely on optical imaging agents. The safety, pharmacokinetics, clearance properties, and radiation dosimetry of ^{124}I-cRGDY–PEG–C dots were assessed by serial PET and computerized tomography after intravenous administration in patients. Metabolic profiles and laboratory tests of blood and urine specimens, obtained before and after particle injection, were monitored over a 2-week interval. Findings are consistent with a well-tolerated inorganic particle tracer exhibiting in vivo stability and distinct, reproducible pharmacokinetic signatures defined by renal excretion. No toxic or adverse events attributable to the particles were observed. Coupled with preferential uptake and localization of the probe at sites of disease, these first-in-human results suggest safe use of these particles in human cancer diagnostics.

INTRODUCTION

Near-infrared (NIR) optical imaging technologies are expected to affect minimally invasive surgical procedures and, in turn, patient outcomes by allowing the surgeon to directly visualize sites of malignancy and the extent of local disease dissemination via the direct integration of camera systems with endoscopic tools (*1*, *2*). Nanomaterials, in particular the development of NIR optically active particle probes, are expected to play a key role in this field, designed to improve the sensitivity and accuracy of lesion detection over that of organic dyes. The emergence of such probes, which have been tailored and refined to address metastatic disease detection (*3*) and other key issues, including targeted drug delivery (*4*), pharmacokinetics (PK) (*5*), and immune response to tumors (*6*), has led to promising technological advances defining the forefront of nanomedicine today. Nanoparticle surface versatility and unique physicochemical and biological properties provide new opportunities to probe molecular targets within human subjects (*7*–*9*). Yet, despite myriad preclinical developments (*10*–*12*), advancing such nano-sized agents into the clinic has been limited or nonexistent.

The promise of cancer nanomedicine lies in the generation of biocompatible, multifunctional agents that promise significantly better targeted treatment of disease than is currently achievable (*13*). In some instances, particle-based agents, which may or may not incorporate therapeutic payloads, have been surface-modified with multiple small molecular ligands (that is, peptides) that recognize and bind cancer markers. The creation of actively targeted small particles (that is, sub–10 nm diameter) offers advantages over larger (10 to 100 nm, or higher) passively targeted nanocarriers, because the latter may nonspecifically accumulate within the tumor interstitium owing to the enhanced permeability and retention (EPR) effect (*10*, *14*, *15*). Molecularly targeted particle products may lead to enhanced receptor binding affinity and avidity (*13*, *16*), extended plasma and tumor residence times, improved bioavailability, favorable tumor-to-blood ratios, as well as intracellular delivery via internalization, as opposed to small molecules (*17*).

We have developed hybrid inorganic (silica) particles, termed Cornell dots (C dots), that can be used for positron emission tomography (PET)–optical dual-modality imaging. These ~6- to 7-nm particles were surface-functionalized with the peptide cyclo-(Arg-Gly-Asp-Tyr) (cRGDY) to detect integrin-expressing lesions in human melanoma xenografts (*16*) and in genetically engineered miniswine models with melanoma (*18*). Tumor-targeted C dots exhibited hallmarks of an ideal diagnostic probe in animal models, selectively targeting disease (and metastases) while exhibiting bulk renal clearance. This latter property was achieved by tuning particle sizes below that of the effective renal glomerular filtration size cutoff of 10 nm (*19*, *20*). Particle probe safety was thereby maximized by reducing nonspecific uptake in the reticuloendothelial system (RES), thus abrogating potential off-target toxicities (*16*). In the spontaneous melanoma miniswine model (*18*), C dots improved target-to-background ratios relative to free dyes, using intraoperative optical imaging guidance (*18*). Moreover, higher sensitivity and specificity of the particle tracer relative to the standard-of-care radiotracer, ^{18}F-fluorodeoxyglucose (^{18}F-FDG), were demonstrated.

On the basis of its versatile design properties, active targeting kinetics, and favorable clearance and toxicity profiles, this ultrasmall silica platform could improve image-based diagnostic assessments and intraoperative cancer care. Toward translation of this inorganic class of imaging nanoparticles, we describe herein a first-in-human trial of ~6-nm hybrid core-shell silica nanoparticles, labeled with ^{124}I for PET imaging,

[1]Department of Radiology, Sloan Kettering Institute for Cancer Research, New York, NY 10065, USA. [2]Department of Medical Physics, Sloan Kettering Institute for Cancer Research, New York, NY 10065, USA. [3]Department of Medicine, Sloan Kettering Institute for Cancer Research, New York, NY 10065, USA. [4]Department of Epidemiology and Biostatistics, Sloan Kettering Institute for Cancer Research, New York, NY 10065, USA. [5]Department of Materials Science and Engineering, Cornell University, 330 Bard Hall, Ithaca, NY 14853, USA.
*Present address: Christian-Albrechts-Universität zu Kiel, Molecular Imaging North Competence Center, Am Botanischen Garten 14, 24118 Kiel, Germany.
†Corresponding author. E-mail: bradburm@mskcc.org and ubw1@cornell.edu

and modified with cRGDY peptides for molecular targeting. Furthermore, the hybrid particles are inherently fluorescent, containing the dye, Cy5. ^{124}I-cRGDY–PEG–C dots received U.S. Food and Drug Administration (FDA) Investigational New Drug (IND) approval as a drug for targeted molecular imaging of integrin-expressing cancers (*16*, *21*). Before using these particles as cancer-directed optical probes for intraoperative applications, we conducted this pilot clinical trial to evaluate the PK and clearance profiles of a single-injection particle tracer dose in metastatic melanoma subjects using PET imaging. Safety measures included monitoring of uptake in normal organs, as well as laboratory toxicity indicators. Secondary objectives were to estimate radiation doses and assess plasma and urine metabolic activity. Our data suggest that systemically administered ^{124}I-cRGDY–PEG–C dots are well tolerated, may accumulate at sites of disease, and exhibit a PK signature that is different from those observed for particle sizes greater than ~10 nm inner diameter—one in which bulk renal clearance predominates without significant RES system uptake, making it safer for patients.

RESULTS

Clinical trial design

After FDA approval of a physician-sponsored IND and Institutional Review Board (IRB) approval, a microdosing study was initiated in $n = 5$ human subjects with metastatic melanoma using the hybrid fluorescent silica particle tracer, ^{124}I-cRGDY–PEG–C dots (Fig. 1A). Before radiolabeling, absorption-matched C dot optical spectra in aqueous solution demonstrated brightness enhancement (per dye) as differences in intensity between the emissions of the encapsulated and free dyes (Fig. 1B). The higher quantum efficiency of the encapsulated versus the native dye results from a greater number of photons emitted after NIR light excitation (that is, increased radiative rate), as well as from a decrease in the number of photons lost to alternative nonradiative processes (that is, decreased nonradiative rate) (*22*). The relative brightness, hydrodynamic diameter, and particle concentration administered are in table S1, along with the post-release radiolabeled product criteria (table S2) and long-term stability data (table S3) of representative batches.

The demographics and clinical history of the patient population are summarized in Fig. 1C. Notably, two patients had tumors harboring the V600E BRAF mutation, which is found in 45% of cutaneous melanomas. All five patients received single-dose intravenous injections of about 185 megabecquerels (MBq) (~3.4 to 6.7 nmol) of ^{124}I-cRGDY–PEG–C dots (specific activity range, 27.8 to 57.4 GBq/μmol), which were well tolerated over the study period based on a safety evaluation that included laboratory indications of particle (drug) toxicity and blood and urine specimen analyses. All subjects had whole-body PET–CT (computed tomography) imaging evaluations

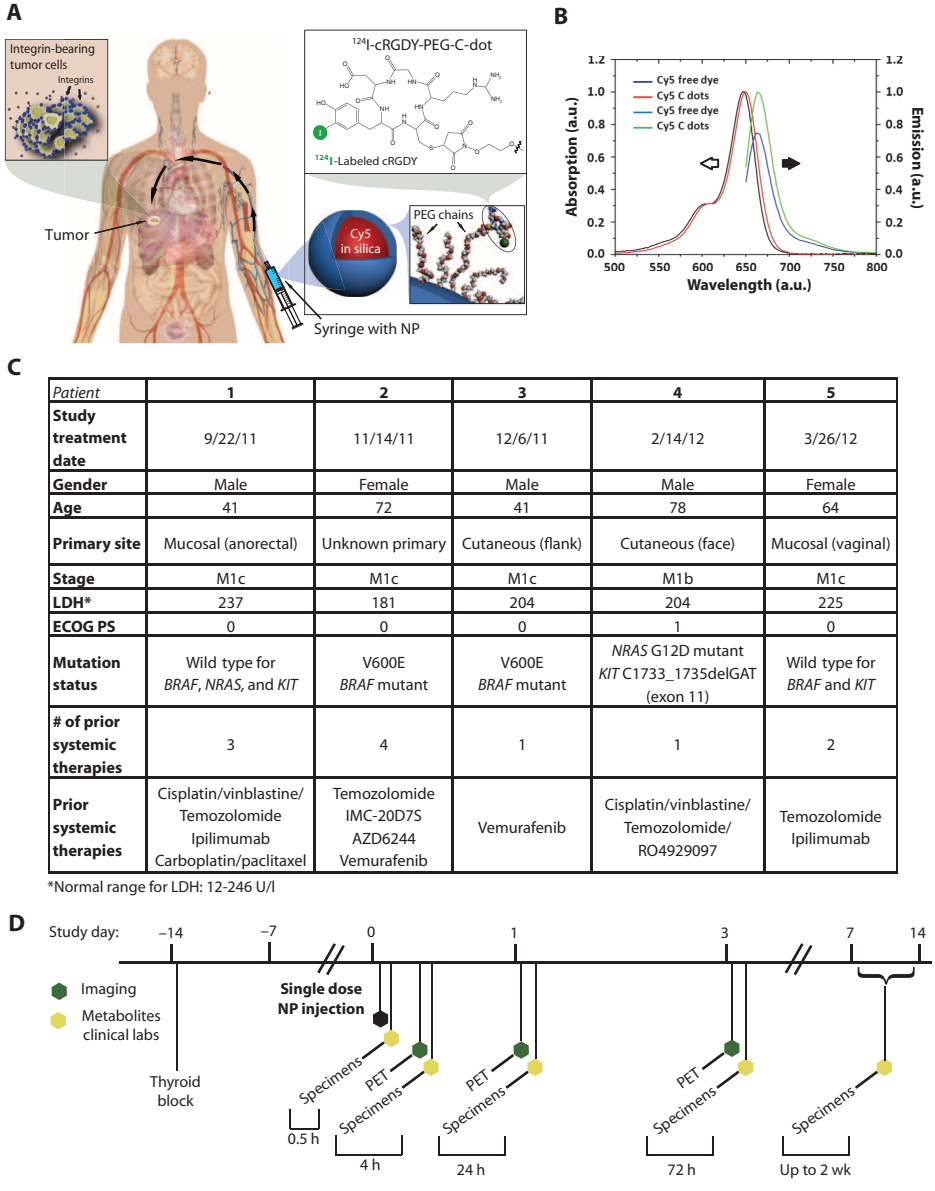

Patient	1	2	3	4	5
Study treatment date	9/22/11	11/14/11	12/6/11	2/14/12	3/26/12
Gender	Male	Female	Male	Male	Female
Age	41	72	41	78	64
Primary site	Mucosal (anorectal)	Unknown primary	Cutaneous (flank)	Cutaneous (face)	Mucosal (vaginal)
Stage	M1c	M1c	M1c	M1b	M1c
LDH*	237	181	204	204	225
ECOG PS	0	0	0	1	0
Mutation status	Wild type for *BRAF*, *NRAS*, and *KIT*	V600E *BRAF* mutant	V600E *BRAF* mutant	*NRAS* G12D mutant *KIT* C1733_1735delGAT (exon 11)	Wild type for *BRAF* and *KIT*
# of prior systemic therapies	3	4	1	1	2
Prior systemic therapies	Cisplatin/vinblastine/ Temozolomide Ipilimumab Carboplatin/paclitaxel	Temozolomide IMC-20D7S AZD6244 Vemurafenib	Vemurafenib	Cisplatin/vinblastine/ Temozolomide/ RO4929097	Temozolomide Ipilimumab

*Normal range for LDH: 12-246 U/l

Fig. 1. Core-shell hybrid silica nanoparticles (^{124}I-cRGDY–PEG–C dots) and overview of first-in-human study design. (**A**) Schematic of the hybrid (PET-optical) imaging nanoparticle (NP) probe showing the core-containing Cy5 dye and surface-attached poly(ethylene glycol) (PEG) chains that bear cRGDY peptide ligands at their ends and ^{124}I radiolabels. cRGDY binds to human $\alpha_v\beta_3$ integrin–expressing tumors. (**B**) Absorption-matched spectra (left, open black arrow) and emission spectra (right, solid black arrow) for free and encapsulated dyes. a.u., arbitrary units. (**C**) Patient ($n = 5$) screening evaluation and clinical history. Stage was determined using the 2010 TNM American Joint Committee on Cancer Cutaneous Melanoma staging system. (**D**) Clinical trial events after single-dose particle injection. Timeline denotes acquisition of serial PET-CT imaging studies and collection of blood and urine specimens.

at 2 to 4, 24, and 72 hours after injection to determine organ uptake and clearance profiles of this particle tracer (Fig. 1D). In addition to assessing PK and particle safety, time-dependent changes in plasma and urinary metabolic profiles were measured over a 2-week interval for biostability and particle integrity using gamma counting and radio thin-layer chromatography (radioTLC). IRB policy and FDA regulations did not allow for a more comprehensive design until the safety of this particle-based agent was proven.

Particle tracer PK

Serial whole-body PET and PET-CT PK profiles are illustrated over a 72-hour period for representative patients #3 (Fig. 2A) and #5 (fig. S1); imaging findings are comparable over this time period. Regions of interest (ROIs) were drawn over all major organs and tissues on the PET images for all five patients using the corresponding CT for guidance. The standard uptake values (SUVs)—where SUV is defined as the activity per gram of tissue divided by the administered activity per gram of body mass—were recorded. These data were converted into %ID/g and plotted as a function of time after injection (Fig. 2B). Collectively, these findings showed that tissue activity is relatively low (that is, values shown as 1/1000th of a percent of the injected dose per gram). As an exception, higher accumulated activities were measured within the thyroid gland of patient #2 relative to that measured in other patients (table S4), secondary to a goiter. The higher thyroid activities seen in patient #2 (table S4) might be explained by the fact that this autonomously functioning glandular tissue could not be effectively blocked with potassium iodide (KI) solution. Except for one lesion in patient #2 and a rim of activity about a hepatic lesion in patient #1, tumors were not visualized. However, by design, the current study was not optimized for lesion detection.

A decline of early blood pool activity resulted in minimal retained activity by 72 hours in all major organs and tissues. Whole-body clearance half-times were estimated to range from 13 to 21 hours. No notable accumulation was observed in the RES, in contrast to many hydrophobic molecules, proteins, and larger-particle (>10 nm) platforms (*10*). The data indicate that a large fraction of the administered activity was eliminated via the urinary system (Fig. 2B). Gamma counting of plasma samples demonstrated biexponential clearance (Fig. 2B); the more rapid initial half-time (that is, $t_{1/2,1}$ ~3.75 hours) was attributed to renal excretion, whereas hepatobiliary clearance presumably accounted for the slower-clearing component. Median %ID/g values and associated interquartile ranges for the intravenously injected particle tracer were tabulated for all major tissues, and for blood and urine specimens over 72 hours (tables S4 and S5).

Metabolic analyses

Metabolic analyses of blood and urine specimens by gamma counting revealed at least an order of magnitude drop in tracer activity over the first 72 hours after injection for all five patients, with minimal C dot activity remaining at the end of this interval (Fig. 3A). Particle activity was largely confined to the blood plasma fraction in this patient cohort. RadioTLC analyses of plasma samples revealed a single peak through 24 hours after injection (Fig. 3B and fig. S2), corresponding to the intact radiolabeled nanoparticle. In urine specimens, two peaks—one corresponding to the intact nanoparticle, and the other to a more mobile species (identified as free iodine)—were seen over a 24-hour period (Fig. 3C and fig. S3). RadioTLC analyses of the particle tracer, with radio-iodinated peptide (^{131}I-cRGDY) and free radioiodine (^{131}I) as standards (Fig. 3D), confirmed that the first and second peaks in the radiochromatograms corresponded to the intact nanoparticle and free iodine, respectively. The size of the second free radioiodide peak in Fig. 3C suggests that the particle was undergoing deiodination. However, this is not the case, because the peak is due to early clearance of ~9% free iodide present in the injected particle preparation, as determined by radioTLC.

On the basis of the estimated total plasma, total-body extracellular fluid (ECF) space, urine activities, and the TLC-based radiochemical analyses of plasma and urine, the percentage of the total activity representing free iodide was very small

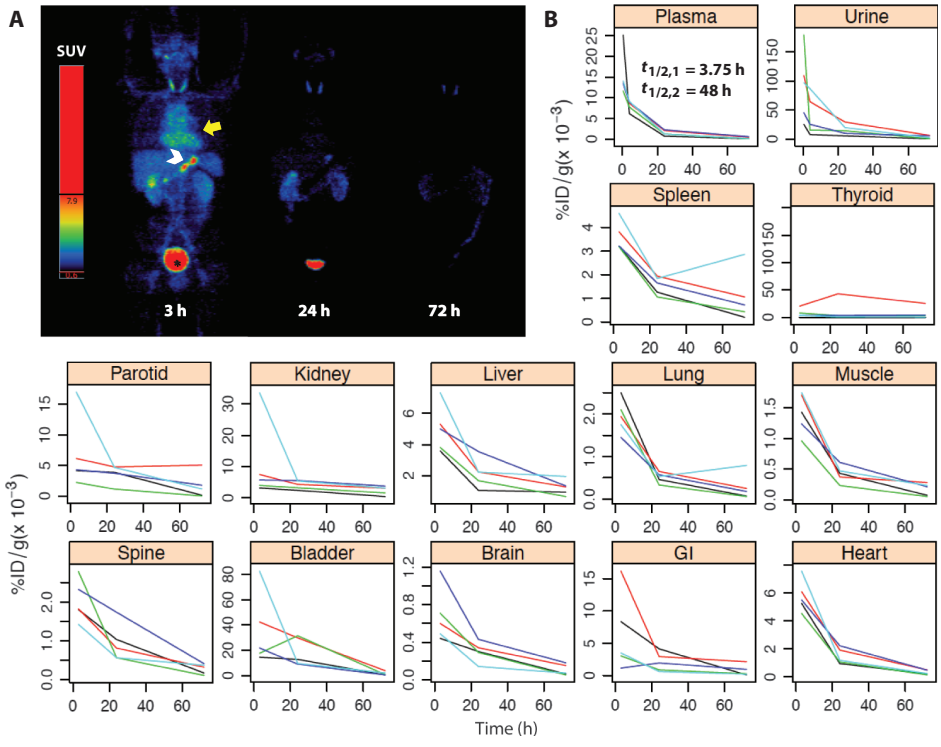

Fig. 2. Whole-body distribution and PK of ^{124}I-cRGDY–PEG–C dots. (**A**) Maximum intensity projection PET images at 2, 24, and 72 hours after intravenous injection of ^{124}I-cRGDY–PEG–C dots (patient #3) reveal probe activity in bladder (*), heart (yellow arrow), and bowel (white arrowhead), displayed as SUV values. (**B**) Decay-corrected percent injected dose per gram (%ID/g) of urine and plasma collected at about 30 min, 4 hours, 24 hours, and 72 hours after injection of the particles as determined by gamma counting. ROIs were drawn on major organs for each patient's PET scans to derive standardized uptake values and %ID/g. Data for major organs and tissues are plotted individually for $n = 5$ patients. Plasma clearance half-times, $t_{1/2,1}$ and $t_{1/2,2}$, are attributed to renal and hepatobiliary clearance, respectively.

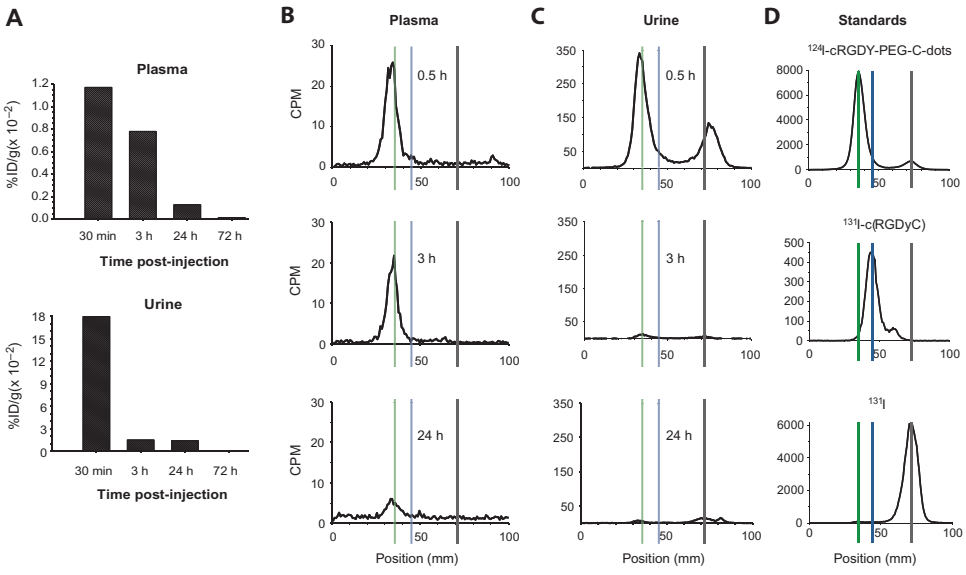

Fig. 3. Metabolic analyses of biological specimens. Data are shown for patient #3. (**A**) Time-dependent activity concentrations (%ID/g × 0.01) in plasma and urine, decay-corrected to the time of injection. (**B** and **C**) RadioTLC (4:1 acetic acid/methanol as mobile phase) of plasma (B) and urine (C) specimens [decay-corrected counts per minute (CPM)]. Data are shown for 0.5-, 3-, and 24-hour time points. (**D**) Chromatograms of standards: injectate, radio-iodinated (^{131}I) peptide, and free ^{131}I. Vertical lines discriminate peaks corresponding to the particle tracer (long dashes; $R_f = 0.04$), ^{131}I-cRGDY (short dashes; $R_f = 0.2$), and ^{131}I (dotted; $R_f = 0.7$). Data for remaining patients are shown in figs. S1 and S2.

(<2.5%) relative to that in the form of intact particle (>97.5%) (table S6), because free iodide freely exchanges between the ECF and plasma compartments. These data indicate that no substantial loss of radiolabel occurred during the study. Similar findings were obtained for this particle tracer by radioTLC in our earlier preclinical work (*16*), where relatively low percent cumulative dehalogenation values (~10%) were measured in urinary specimens of murine melanoma models over 24 hours. In addition, given the absence of peaks corresponding to particle breakdown products, the radiochromatograms showed no evidence of instability of the particle itself. This is consistent with the results of our earlier murine melanoma studies that showed no significant loss of particle integrity over a 24-hour period after injection in urine specimens by fluorescence correlation spectroscopy, relative to preinjection values (*16*).

Radiation dosimetry

Organ-absorbed doses and the effective dose for each patient, along with the mean organ absorbed dose for all patients, are presented in Fig. 4. The mean dose for all patients was comparable to that for other commonly used diagnostic radiotracers administered at comparable injected activities, for instance, doses of the order of 1 mGy/MBq. In addition, the average effective dose in human subjects, 0.183 ± 0.065 mSv/MBq (range, 0.115 ± 0.278 mSv/MBq), was comparable to that estimated from our earlier preclinical data (~0.157 mSv/MBq) (*16*). Patients were pretreated with KI to block thyroid tissue uptake, and thus, there was only a low concentration of free iodide activity in the thyroid [KI blockade typically blocks >95% of iodide uptake, but rarely achieves 100% blockade (*23*)]. The mean thyroid dose was ~0.7 mGy/MBq, which is less than 1% of the thyroid dose due to free ^{124}I. As noted, particles were also primarily excreted by the kidneys, with both kidney and bladder wall (after thyroid gland) demonstrating two of the highest mean absorbed dose values 72 hours after injection compared to other tissues (Fig. 4).

Image-derived time-activity data were used to estimate the median cumulated activities (or total ^{124}I disintegrations) of the particle tracer in all major organs and tissues, along with their associated SDs (table S7). Despite muscle and bone having low activity concentrations through 72 hours after injection (Fig. 2B), these tissues had surprisingly high cumulative activities. This, however, may be a result of muscle and bone having larger total masses, thus resulting in relatively larger cumulative activities than other organs.

Multimodal imaging with ^{124}I-cRGDY–PEG–C-dots: Clinical case studies

Although the current microdosing trial was not designed as a tumor-targeting study (that is, no attempt was made to adjust particle doses to optimize tumor targeting), lesion uptake and localization were seen in several patients along with a case of renal inflammation. A whole-body PET-CT scan was acquired 4 hours after intravenous administration of ^{124}I-cRGDY–PEG–C-dots in patient #1, who had anorectal mucosal melanoma and a known liver metastasis within the inferior left lobe. On coronal CT images (Fig. 5A), a large area of decreased density was seen in the inferior left lobe of the liver, at the site of the known metastatic lesion. On the coronal PET (Fig. 5B) and co-registered PET-CT scans (Fig. 5C), particle uptake appeared to circumscribe the liver lesion (Fig. 5, B and C) and subsequently cleared by the time of the 24-hour PET scan (Fig. 5D), suggesting some localization in this metastasis. Particle activity was seen within the bladder, gastrointestinal tract (stomach, intestines), heart, and the gallbladder (Fig. 5, B and C). An ^{18}F-FDG PET scan (Fig. 5D) acquired several days later showed a hepatic metastasis with a more hypermetabolic tumor border, corresponding to that seen in Fig. 5B. Although the lesion demonstrated more prominent ^{18}F-FDG activity, this reflects a different aspect of tumor biology, namely, glucose transport and metabolism. ^{124}I-cRGDY–PEG–C dot uptake would reflect integrin biology.

In patient #2, injected intravenously with ^{124}I-cRGDY–PEG–C dots, a ~5-mm well-defined cystic lesion was seen in the right anterior lobe of the pituitary gland, which lacks a blood-brain barrier, on axial and sagittal magnetic resonance (MR) images (Fig. 6A). This lesion, a stable finding on previous MR imaging (MRI) scans, was presumed to be a pituitary microadenoma—an intracranial neoplasm known to exhibit malignant properties, such as neoangiogenesis and progression into peritumoral tissues. Precise co-registration of this tracer-avid focus with multiplanar MRI (Fig. 6B) and CT (Fig. 6C) images confirmed its location within the anterior pituitary gland. Initially seen as a focus of intense activity, it progressively increased in intensity over a 72-hour interval (arrow, Fig. 6D), accompanied by a corresponding decrease in

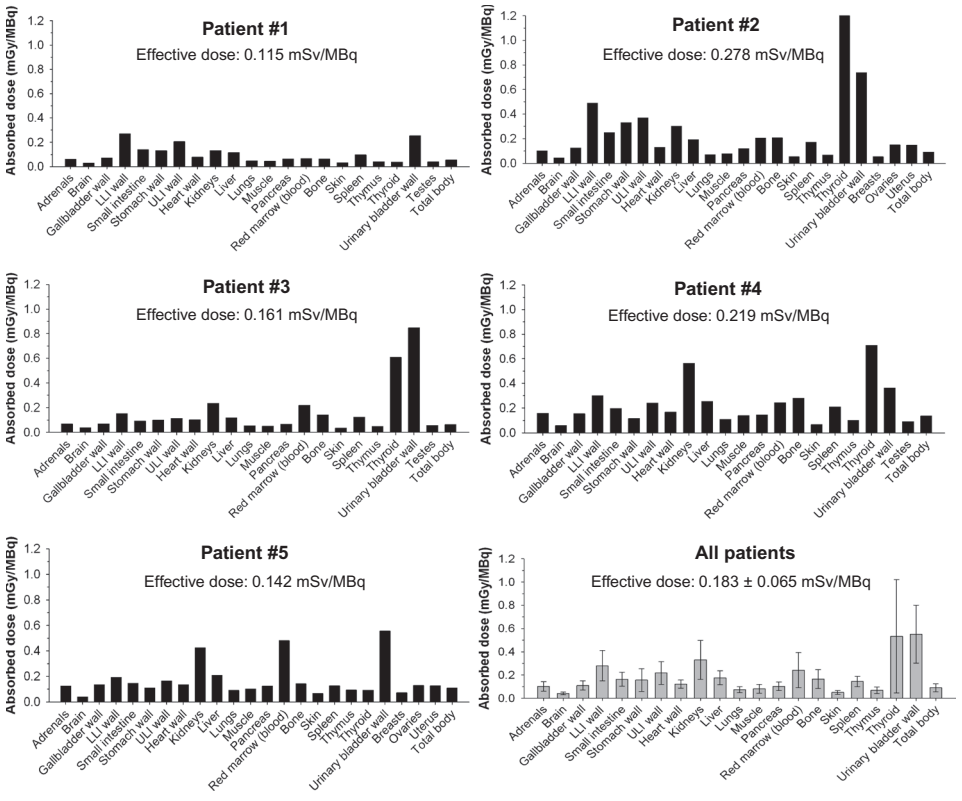

Fig. 4. Dosimetry of ^{124}I-cRGDY–PEG–C dots. Absorbed doses per unit administered activity (mGy/MBq) of major organs and tissues were derived for each patient ($n = 5$) from serial whole-body PET scans acquired over a 72-hour time interval after injection of the particle tracer and using ROI-based time-activity data. Data are also displayed as averages ± SD in the gray-colored bar graph for all patients.

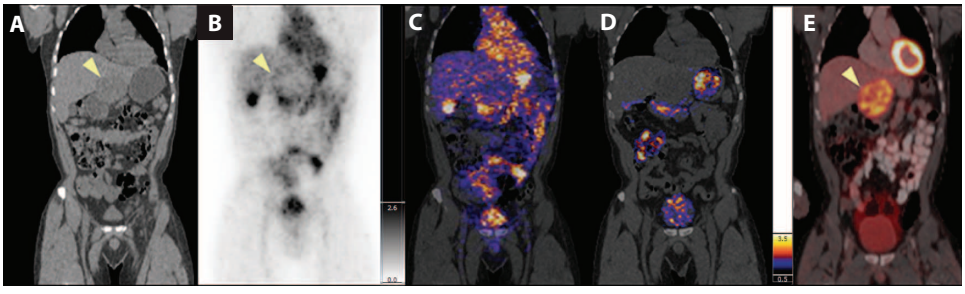

Fig. 5. Whole-body PET-CT imaging of particle biodistribution and tumor uptake after systemic injection of ^{124}I-cRGDY–PEG–C dots. (**A**) Reformatted coronal CT in patient #1 demonstrates a hypodense left hepatic lobe metastasis (arrowhead). (**B**) Coronal PET image at 4 hours after injection demonstrates particle activity along the peripheral aspect of the tumor (arrowhead), in addition to the bladder, gastrointestinal tract (stomach, intestines), gallbladder, and heart. (**C** and **D**) Co-registered PET-CT at 4 hours (C) and 24 hours (D) after injection localizes activity to the tumor margin. (**E**) Corresponding ^{18}F-FDG PET-CT image showing the hepatic metastasis in (A) (arrowhead). Color and gray scales reflect SUV values.

surrounding background signal, thus yielding high tumor-to-background (to-brain ~500; to-liver ~50) ratios (Fig. 6E). Because the lesion diameter was slightly less than the resolution (full-width half-maximum ~6 mm) of the clinical PET scanner, these ratios had to be corrected for partial volume effects (*24*). This increase in signal reflects a net accumulation of particle activity within the lesion over time.

The fraction of the injected particle load that accumulated at the tumor site was evaluated for patient #2 (Fig. 6D). Using the measured maximum SUV (SUV_{max}) of the lesion (46.5) at 72 hours after injection (which was nearly an order of magnitude higher than that of normal pituitary tissue), the approximate mass of the lesion, and the patient's body mass, we found that, relative to an injected particle load of 2×10^{15}, roughly 1.78×10^{11} particles, or 0.01%, of the injected dose accumulated at the lesion site.

In patient #4, who had a history of impaired renal function and mildly elevated creatinine levels (table S8) related to chemotherapy (cisplatin)–related nephrotoxicity, prolonged ^{124}I-cRGDY–PEG–C dot activity was observed in both renal cortices over several days (Fig. 7A). Similar to PET findings in the first subject (Fig. 5B), prominent activity, or radiation emission, was initially noted at 3 hours after injection within the cardiac blood pool, gastrointestinal tract, and glandular structures, followed by renal clearance and accumulation in the urinary bladder. Over the next 72 hours, activity was seen to persist in the renal cortices. Reformatted sagittal and axial CT images 72 hours after particle injection (Fig. 7B) demonstrated perinephric stranding about both kidneys, without evidence of hydronephrosis or hydroureter. This likely reflected inflammatory sequelae, because similar findings were present before particle administration. Renal function continued to improve after particle injection, with creatinine levels declining from a value of 1.7 to 1.5 mg/dl (upper limits of normal), the latter value maintained for at least 72 hours (table S8).

Patient safety evaluation

Safety assessments were based on lack of clinical symptoms, absence of any laboratory indications of particle (drug) toxicity, dosimetry, and blood and urine specimen analyses. Blood and urine metabolic profiles are tabulated for male (table S8) and female (table S9) subjects, along with normal parameter ranges. Urinalysis results are shown in table S10. Average blood urea nitrogen and creatinine concentrations, measured to assess renal function (tables S8 and S9), did not substantially change over the 2-week study interval. In one male subject (patient #4, Fig. 7) with a history of acute drug-induced nephritis, mildly elevated parameter values found before particle administration were noted to decrease over at least a 72-hour window, indicating a non-obstructive uropathy. These findings provided evidence that renal function was unaffected by the particle tracer. To assess alterations in liver function, liver panel assessments were conducted to assay aspartate aminotransferase, alanine transaminase, alkaline

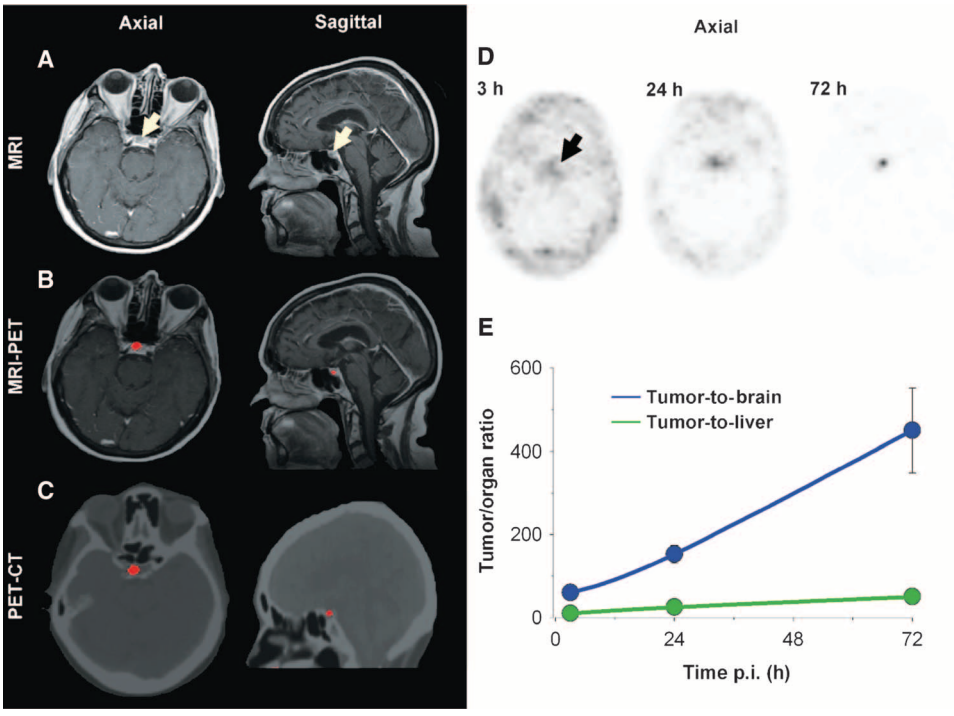

Fig. 6. Multimodal imaging of particle uptake in a pituitary lesion. (**A**) Multiplanar contrast-enhanced MR axial and sagittal images of patient #2 at 72 hours after injection demonstrate a subcentimeter cystic focus (arrows) within the right aspect of the anterior pituitary gland. (**B**) Co-registered axial and sagittal MRI-PET images reveal increased focal activity (red, ^{124}I-cRGDY–PEG–C dots) localized to the lesion site. (**C**) Axial and sagittal PET-CT images localize activity to the right aspect of the sella. (**D**) Axial PET images of ^{124}I-cRGDY–PEG–C dots in the brain at 3, 24, and 72 hours after injection demonstrate progressive accumulation of activity within the sellar region. (**E**) Tumor-to-brain and tumor-to-liver activity ratios as a function of post-injection (p.i.) time. Data are averages ± SD (n = 1 ROI measurement per time point) calculated from images in (D).

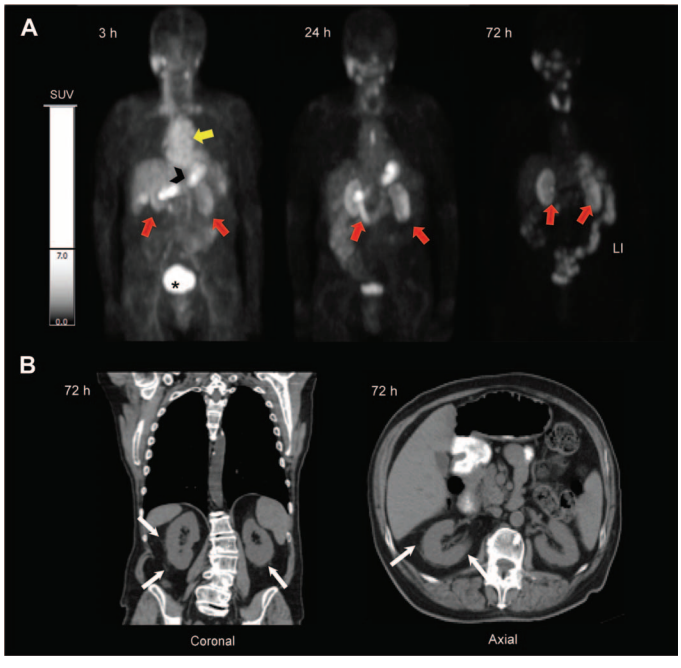

Fig. 7. PET imaging of particle uptake in a patient with drug-induced nephrotoxicity. (**A**) Serial PET coronal images of patient #4 acquired at 3, 24, and 72 hours after injection demonstrate initial presence of ^{124}I-cRGDY–PEG–C dots within the cardiac blood pool (yellow arrow), small bowel (black arrowhead), and renal excretion, with accumulated urinary bladder activity (asterisk) and retention of activity in both renal cortices (red arrows). (**B**) Corresponding multiplanar CT sagittal and axial images at 72 hours after injection. White arrows point to perinephric stranding.

phosphatase, albumin, total bilirubin, and total protein levels. No changes in liver function were found to be attributable to particle infusion.

The laboratory assessment of drug toxicity observed at baseline or within 2 weeks of therapy (table S11), graded according to the National Cancer Institute's Common Terminology Criteria for Adverse Events (CTCAE, v4.0), suggested that adverse events were unrelated to particle injection and that the particle was safe. These findings were based on an absence of substantial changes in laboratory values over the 2-week period relative to those measured before particle injection.

DISCUSSION

This first-in-human clinical study represents the translation of cancer-targeted, renally excreted inorganic nanoparticles for PET and optical imaging from mouse to man. There is a strong desire for the use of nanoparticles, including silica (inorganic), gold (metallic), and quantum dots (semiconductor materials), in the clinic for targeted imaging and drug delivery. These, however, should have properties of an ideal cancer-targeting probe, having overcome barriers related to renal clearance, toxicity, and nonspecific biodistribution. C dots are ultrasmall (<10 nm), integrin-targeting nanoparticles that have been tuned to sizes that promote renal excretion and limit nonspecific RES uptake, thus enhancing bioavailability and minimizing off-target toxicity. Our data here in five melanoma patients indicate favorable PK/biodistribution profiles and safety of this targeted, inorganic imaging agent, thus opening the door for the use of other, similar nanoparticles in humans.

Targeted C dots were initially approved for use as a particle tracer and not as an optical probe for image-guided surgeries. Hence, the primary objective of this pilot study was to assess safety and to quantitatively monitor whole-body tissue distributions and clearance of ^{124}I-cRGDY–PEG–C dots using quantitative PET imaging and low clinical tracer doses. Acquired PK profiles were examined for reproducibility among subjects and used to derive human plasma and whole-body clearance half-times. The results obtained from this proof-of-concept clinical study point to an inorganic particle

tracer that was safe and exhibited reproducible PK signatures defined by renal excretion—in contrast to the slower clearance of other larger PET particle systems. In contrast to C dot whole-body clearance half-time values (that is, 13 to 21 hours), ^{111}In-labeled liposomes ~90 nm inner diameter were found to have median clearance half-time values ranging from 40 to 103 hours in patients with locally advanced malignancies (*25*). In this latter instance, a biodistribution pattern was also seen within the liver, spleen, and bone marrow, consistent with RES uptake. In another study recruiting patients with colorectal carcinoma (*26*), whole-body clearance half-time values of ^{131}I-labeled humanized monoclonal antibody A33, twice the C dot diameter, ranged from 120 to 176 hours. Thus, the use of ultrasmall C dots, on the order of the effective renal glomerular filtration size cutoffs (*19*), was critical to achieving the foregoing results.

Although PK signature is a function of the particle size, other physicochemical properties, including charge, shape, and surface chemistry, also modulate PK. In an earlier mouse study, we showed that most C dots (<10 nm) without a PEG coat ended up in the liver (*20*); by contrast, ^{124}I-cRGDY–PEG–C dots were cleared by the urinary system. As a result, PK data reported in the literature will differ among different macromolecules (albumin) (*27*) or other particle types (gold nanoparticles) (*28*) exhibiting diameters similar or smaller in size than the particles used here. Further, the PK signature of ^{124}I-cRGDY–PEG–C dots differed from those of RES agents and antibodies, because no appreciable particle tracer accumulation was seen within the liver, spleen, lung, or bone marrow.

Particle tracer distributions, clearance, and dosimetric profiles were similar to those found in our preclinical melanoma models (*16*). Bladder activity concentrations were nearly an order of magnitude higher than those in the liver. On the basis of the conservative assumption that all hepatic activity is ultimately excreted via the hepatobiliary route, these data are consistent with ~90% of the administered activity being excreted via the kidneys and ~10% via the hepatobiliary route. The route of excretion is a consideration in developing particle tracers because gut activity can potentially confound image interpretation; for ^{124}I-cRGDY–PEG–C dots, this was minimized. Moreover, particle PK and estimated organ effective doses were comparable to those found for other commonly used diagnostic radiotracers (~1 mSv/MBq).

PK findings were also in line with $\alpha_v\beta_3$ integrin expression levels in most normal tissues, which demonstrate a concentration-dependent distribution: low-level expression, for instance, is found in tissues of intestinal and vascular origin (*29*). Although the gastrointestinal tract was visualized, the activity-concentration therein was low (that is, <0.001%/g). On the basis of previous cRGD radiotracer literature (*30*), there was no unexpected localization of particle activity within the body. A small fraction of the dose, however, was seen as uptake in the stomach and salivary glands; this was presumed to be free iodide already present in the injected particle preparation or cleaved from the particle by dehalogenases (vide infra). Such enzymatic dehalogenation occurs to a variable degree for all radioiodinated pharmaceuticals. Very low accumulated activity within the thyroid gland, which cleared over the study interval, was thought to reflect a combination of free iodide and iodide in particulate form. In the latter case, it is known that integrin receptors are expressed at low density within the thyroid gland, with uptake of dimeric peptides observed previously (*31*).

Most activity measured in the plasma, urine, and total-body ECF was in the form of particle tracer, not free iodide. Free iodide exchange occurs between the ECF and the plasma compartment (*32*). Thus, sampling and radioTLC of plasma disclosed not only plasma-borne iodide but also total-body (nonthyroidal) iodide, because plasma is part of the total-body ECF with respect to free iodide. It can also be stated that (extrathyroidal) organ radioactivity will be a reflection of that contained within the plasma compartment. Thus, if the overall percentage of free iodide activity in the plasma is low at 24 hours, corresponding parenchymal organ activities will also be low (Fig. 2).

These findings support the notion that the particle tracer is stable in vivo and that PET imaging follows the particle distribution (*33*). The observed rapid renal clearance is predominantly driven by the kinetics of the particle itself. The free iodide contribution to the overall activity, measured at 0.5 hour by radioTLC (Fig. 3C), likely reflected early clearance of free iodide present in the injected particle preparation (~9% of total injected activity) and was consistent with free iodide in the injectate being rapidly cleared from plasma (8.7-hour plasma-to-urine clearance half-time) (*34*).

Clinical PET imaging of ^{124}I-cRGDY–PEG–C dots

Use of image-guided biopsy procedures to acquire tumor tissue specimens as part of a more comprehensive trial design was precluded on the basis of IRB policy and FDA regulations until particle safety was proven. Furthermore, anatomic sites of disease identified in these patients were, on the whole, not easily accessed, increasing biopsy risk. We were therefore unable to match histology with imaging data. Nonetheless, it is important to consider biological mechanisms that may contribute to retained particle activity seen with in vivo PET imaging, particularly in light of the measured clearance profiles. It is important to highlight the ability of PET to accurately estimate the fraction of the injected particle load that accumulates at tumor sites, in addition to monitoring time-varying particle uptake (*35*). There is no PET label available with a half-life longer than that of ^{124}I for radiolabeling control (non–RGDY-bearing) C dots; therefore, we could not quantify nonspecifically localized C dots (for example, due to the EPR effect) in the patients. Future trials with a larger number of patients should address such issues.

Despite the low nanomolar amounts used and lack of optimization of dosing, accumulation of the particle tracer occurred in the lesions of several subjects. In patient #2, who had a presumed pituitary adenoma, PET imaging showed a progressive net accumulation of ^{124}I-cRGDY–PEG–C dot activity at the lesion site (Fig. 6D). Such progressively increasing lesion activity was consistent with specific uptake, although the actual integrin receptor expression status was unknown. Previous studies investigating altered integrin expression levels associated with adenomatous transformation (*36*) have shown enhanced $\alpha_v\beta_3$ integrin expression levels primarily involving adenomatous stromal cells, as well as the parenchyma of adenomas, which may explain this finding in our study.

In patient #4, who had a history of cisplatin-related nephrotoxicity and acute renal disease, cortical retention of particle activity was observed. Radiographic findings were not consistent with an obstructive uropathy, and there was no clinical evidence of active renal disease during the study interval. However, soft tissue stranding about both kidneys on CT images suggested the sequelae of an inflammatory process. The inflammatory aspects of nephrotoxicity, secondary to toxicants such as cisplatin, are well documented (*37*, *38*) and are known to critically involve the vasculature. Sites of inflammation recruit leukocytes via the post-capillary venules, a process dependent on the activation and enhanced expression of cell adhesion molecules, including integrins (*38*). In this setting, retained renal cortical activity might reflect sites of preferential localization and accumulation of integrin-binding particles.

cRGDY is a cyclic peptide that targets integrin $\alpha_v\beta_3$, which is highly expressed on activated endothelial cells involved in angiogenesis and vascular remodeling, as well as on solid tumor cells; it is not expressed on mature vessels or on nonneoplastic epithelium (*39*). Hence, our radiolabeled cRGDY particle conjugate, coupled with clinical PET imaging, could select patients for integrin-targeted treatments, provide noninvasive imaging of tumor cells and neovasculature, and monitor treatment efficacy. The specific biological information supplied by such particle tracers could complement that acquired by nonspecific radiopharmaceuticals, such as ^{18}F-FDG, which is commonly used to screen for and stage tumors, including melanoma. The data in this study may be extended to treatment management settings for estimating particle dosing requirements in the context of image-guided surgeries or therapeutic interventions. In the future, ultrasmall ^{124}I-cRGDY–PEG–C dots can be surface-functionalized with different targeting moieties, tailored to meet individual patient needs, and thus pave the way toward improving patient care.

MATERIALS AND METHODS

Study design

A microdosing clinical trial was conducted at Memorial Sloan Kettering Cancer Center (MSKCC) after approval by the IRB of MSKCC and the FDA in conjunction with a physician-sponsored IND (no. 110375). The trial was registered in the Clinical Trials Registry (http://clinicaltrials.gov/; NCT01266096), and a Clinical Research Database at MSKCC was established to record adverse events. All patients provided informed consent.

The overall objective was to perform a nonblinded pilot study in melanoma patients after single-dose injection of ^{124}I-cRGDY–PEG–C dots to characterize their biodistribution, PK, metabolic stability, and dosimetry. Because ^{124}I-cRGDY–PEG–C dots had not been previously administered to humans, the foregoing studies were conducted in a small cohort ($n = 5$) of subjects with limited life expectancy, as required by the FDA before initiating conventional dose escalation phase 1 trials designed to optimize tumor-targeting kinetics. Hence, for this study, metastatic melanoma subjects (>18 years), with histological confirmation of disease, and who harbored newly diagnosed or recurrent tumor, or had residual clinically or radiographically evident tumor, including primary cutaneous and mucosal melanomas, were recruited (Fig. 1C). Additional inclusion criteria included normal hematologic, hepatic, and cardiac function. Individuals who had medical illness unrelated to melanoma, which would preclude administration of the particle tracer, including those with uncontrolled infection, chronic renal failure, chronic active hepatitis, and unstable cardiac disease, were excluded from participating in the study. Potential patients with active thyroid disease were also excluded. An IRB waiver was approved for one subject with a recent history of acute drug-induced nephritis and mildly impaired renal function (creatinine value of 1.7) on the basis of the institution's previous radiopharmaceutical experience in these populations and potential risk to the patient.

A single particle tracer dose (185 MBq) was administered intravenously. KI solution (130 mg/day) was self-administered orally 2 days before and up to 2 weeks after intravenous injection of the radioiodinated particle tracer to block uptake of free iodine by the thyroid. Serial PET-CT imaging studies ($n = 3$ per patient) were used to establish whether the particle probe exhibited key in vivo characteristics desirable of a diagnostic PET radiotracer, including bulk renal clearance, low background signal, stability, biosafety, and acceptable mean absorbed radiation doses. Blood and urine specimens were collected from patients for assessment of metabolites, chemistries, and hematologic, renal, and liver function after each of the acquired PET imaging studies, and up to 2 weeks after injection. All patients were observed clinically after probe injection over this time interval. The PK, dosimetry, and laboratory data collected at each time point were single measurements. Laboratory toxicity was graded using the CTCAE (v4.0). Results were compared with each subject's baseline values and standardized normal values to verify that no demonstrable alterations attributable to particle administration occurred.

Synthesis and characterization of ^{124}I-cRGDY–PEG–C dots

The synthesis and characterization of PEG and cRGDY surface-functionalized fluorescent core-shell silica nanoparticles (cRGDY–PEG–C dots) have been described previously (*16*) and are elaborated upon with radioiodination in Supplementary Materials and Methods.

PK and metabolic analyses

ROIs were drawn on PET imaging data (AW Workstation, GE Healthcare) to extract mean and maximum SUVs for all major normal organs and tissues, including brain, lung, left ventricle, liver, spleen, intestine, kidneys, bladder, muscle, breast, and tumor(s). Organ and tissue uptake data were supplemented by time-activity data from the blood and urine. Detailed methods are in the Supplementary Materials.

PET imaging

PET images were recorded for each patient at 4, 24, and 72 hours after injection of the particle tracer. Image acquisition and processing are described in the Supplementary Materials.

Statistical analyses

Summary statistics (mean, median, SD, and interquartile ranges) for %ID/g values were estimated using the sample mean, sample SD, and sample quartiles (*40*). Given the small patient sample size, all data values were presented in tabular and/or graphical formats. All statistical analyses were conducted using R (version 2.15, http://www.r-project.org), and multipanel time profiles of %ID/g were generated using the lattice package (*41*).

SUPPLEMENTARY MATERIALS

www.sciencetranslationalmedicine.org/cgi/content/full/6/260/260ra149/DC1

Materials and Methods

Fig. S1. Whole-body PET-CT imaging biodistributions of ^{124}I-cRGDY–PEG–C dots with time.

Fig. S2. RadioTLC chromatograms of plasma specimens and standards.

Fig. S3. RadioTLC chromatograms of urinary specimens and standards.

Table S1. Photophysical characterization of cRGDY–PEG–C dots by fluorescence correlation spectroscopy.

Table S2. Post-release product criteria for cRGDY–PEG–C dots.

Table S3. Stability measurements of cRGDY–PEG–C dot batches ($n = 2$) by fluorescence correlation spectroscopy.

Table S4. Individual patient PK results for intravenously injected ^{124}I-cRGDY–PEG–C dots.

Table S5. Summary of PK results for ^{124}I-cRGDY–PEG–C dots delivered by systemic injection.

Table S6. Percentage of total body activity of ^{124}I-labeled nanoparticle or free iodide (^{124}I).

Table S7. Organ- and tissue-specific cumulative ^{124}I activities by patient.

Table S8. Complete metabolic profile in male subjects.

Table S9. Complete metabolic profile in female subjects.

Table S10. Analysis of urine specimens.

Table S11. Hematologic and nonhematologic adverse events.

References (*42*–*46*)

REFERENCES AND NOTES

1. R. Weissleder, M. J. Pittet, Imaging in the era of molecular oncology. *Nature* **452**, 580–589 (2008).
2. S. Gioux, H. S. Choi, J. V. Frangioni, Image-guided surgery using invisible near-infrared light: Fundamentals of clinical translation. *Mol. Imaging* **9**, 237–255 (2010).
3. A. Schroeder, D. A. Heller, M. M. Winslow, J. E. Dahlman, G. W. Pratt, R. Langer, T. Jacks, D. G. Anderson, Treating metastatic cancer with nanotechnology. *Nat. Rev. Cancer* **12**, 39–50 (2011).
4. R. Duncan, The dawning era of polymer therapeutics. *Nat. Rev. Drug Discov.* **2**, 347–360 (2003).
5. D. A. Scheinberg, C. H. Villa, F. E. Escorcia, M. R. McDevitt, Conscripts of the infinite armada: Systemic cancer therapy using nanomaterials. *Nat. Rev. Clin. Oncol.* **7**, 266–276 (2010).
6. T. H. Kim, S. Lee, X. Chen, Nanotheranostics for personalized medicine. *Expert Rev. Mol. Diagn.* **13**, 257–269 (2013).
7. J. M. Rosenholm, V. Mamaeva, C. Sahlgren, M. Lindén, Nanoparticles in targeted cancer therapy: Mesoporous silica nanoparticles entering preclinical development stage. *Nanomedicine* **7**, 111–120 (2012).
8. C. E. Ashley, E. C. Carnes, G. K. Phillips, D. Padilla, P. N. Durfee, P. A. Brown, T. N. Hanna, J. Liu, B. Phillips, M. B. Carter, N. J. Carroll, X. Jiang, D. R. Dunphy, C. L. Willman, D. N. Petsev, D. G. Evans, A. N. Parikh, B. Chackerian, W. Wharton, D. S. Peabody, C. J. Brinker, The targeted delivery of multicomponent cargos to cancer cells by nanoporous particle-supported lipid bilayers. *Nat. Mater.* **10**, 389–397 (2011).
9. J. L. Vivero-Escoto, R. C. Huxford-Phillips, W. Lin, Silica-based nanoprobes for biomedical imaging and theranostic applications. *Chem. Soc. Rev.* **41**, 2673–2685 (2012).
10. U. Prabhakar, H. Maeda, R. K. Jain, E. M. Sevick-Muraca, W. Zamboni, O. C. Farokhzad, S. T. Barry, A. Gabizon, P. Grodzinski, D. C. Blakey, Challenges and key considerations of the enhanced permeability and retention effect for nanomedicine drug delivery in oncology. *Cancer Res.* **73**, 2412–2417 (2013).
11. S. Keereweer, P. B. Van Driel, T. J. Snoeks, J. D. Kerrebijn, R. J. Baatenburg de Jong, A. L. Vahrmeijer, H. J. Sterenborg, C. W. Löwik, Optical image-guided cancer surgery: Challenges and limitations. *Clin. Cancer Res.* **19**, 3745–3754 (2013).
12. X. He, J. Gao, S. S. Gambhir, Z. Cheng, Near-infrared fluorescent nanoprobes for cancer molecular imaging: Status and challenges. *Trends Mol. Med.* **16**, 574–583 (2010).
13. W. C. Zamboni, V. Torchilin, A. K. Patri, J. Hrkach, S. Stern, R. Lee, A. Nel, N. J. Panaro, P. Grodzinski, Best practices in cancer nanotechnology: Perspective from NCI nanotechnology alliance. *Clin. Cancer Res.* **18**, 3229–3241 (2012).
14. Y. Matsumura, H. Maeda, A new concept for macromolecular therapeutics in cancer chemotherapy: Mechanism of tumoritropic accumulation of proteins and the antitumor agent smancs. *Cancer Res.* **46**, 6387–6392 (1986).
15. S. Svenson, Theranostics: Are we there yet? *Mol. Pharm.* **10**, 848–856 (2013).
16. M. Benezra, O. Penate-Medina, P. B. Zanzonico, D. Schaer, H. Ow, A. Burns, E. DeStanchina, V. Longo, E. Herz, S. Iyer, J. Wolchok, S. M. Larson, U. Wiesner, M. S. Bradbury, Multimodal silica nanoparticles are effective cancer-targeted probes in a model of human melanoma. *J. Clin. Invest.* **121**, 2768–2780 (2011).
17. N. Kamaly, Z. Xiao, P. M. Valencia, A. F. Radovic-Moreno, O. C. Farokhzad, Targeted polymeric therapeutic nanoparticles: Design, development and clinical translation. *Chem. Soc. Rev.* **41**, 2971–3010 (2012).
18. M. S. Bradbury, E. Phillips, P. H. Montero, S. M. Cheal, H. Stambuk, J. C. Durack, C. T. Sofocleous, R. J. C. Meester, U. Wiesner, S. Patel, Clinically-translated silica nanoparticles as dual-modality cancer-targeted probes for image-guided surgery and interventions. *Integr. Biol.* **5**, 74–86 (2013).
19. C. H. Choi, J. E. Zuckerman, P. Webster, M. E. Davis, Targeting kidney mesangium by nanoparticles of defined size. *Proc. Natl. Acad. Sci. U.S.A.* **108**, 6656–6661 (2011).
20. A. A. Burns, J. Vider, H. Ow, E. Herz, O. Penate-Medina, M. Baumgart, S. M. Larson, U. Wiesner, M. Bradbury, Fluorescent silica nanoparticles with efficient urinary excretion for nanomedicine. *Nano Lett.* **9**, 442–448 (2009).
21. J. V. Jokerst, S. S. Gambhir, Molecular imaging with theranostic nanoparticles. *Acc. Chem. Res.* **44**, 1050–1060 (2011).
22. D. R. Larson, H. Ow, H. D. Vishwasrao, A. A. Heikal, U. Wiesner, W. W. Watt, Silica nanoparticle architecture determines radiative properties of encapsulated fluorophores. *Chem. Mater.* **20**, 2677–2684 (2008).
23. P. Verger, A. Aurengo, B. Geoffroy, B. Le Guen, Iodine kinetics and effectiveness of stable iodine prophylaxis after intake of radioactive iodine: A review. *Thyroid* **11**, 353–360 (2001).
24. M. Soret, S. L. Bacharach, I. Buvat, Partial-volume effect in PET tumor imaging. *J. Nucl. Med.* **48**, 932–945 (2007).
25. S. Stewart, K. J. Harrington, The biodistribution and pharmacokinetics of stealth liposomes in patients with solid tumors. *Oncology* **11** (Suppl. 11), 33–37 (1997).
26. A. M. Scott, F. T. Lee, R. Jones, W. Hopkins, D. MacGregor, J. S. Cebon, A. Hannah, G. Chong, P. U, A. Papenfuss, A. Rigopoulos, S. Sturrock, R. Murphy, V. Wirth, C. Murone, F. E. Smyth, S. Knight, S. Welt, G. Ritter, E. Richards, E. C. Nice, A. W. Burgess, L. J. Old, A phase I trial of humanized monoclonal antibody A33 in patients with colorectal carcinoma: Biodistribution, pharmacokinetics, and quantitative tumor uptake. *Clin. Cancer Res.* **11**, 4810–4817 (2005).
27. G. Stehle, A. Wunder, H. H. Schrenk, G. Hartung, D. L. Heene, H. Sinn, Albumin-based drug carriers: Comparison between serum albumins of different species on pharmacokinetics and tumor uptake of the conjugate. *Anticancer Drugs* **10**, 785–790 (1999).
28. A. Leifert, Y. Pan-Bartnek, U. Simon, W. Jahnen-Dechent, Molecularly stabilised ultrasmall gold nanoparticles: Synthesis, characterization and bioactivity. *Nanoscale* **5**, 6224–6242 (2013).
29. R. L. Wilder, Integrin alpha V beta 3 as a target for treatment of rheumatoid arthritis and related rheumatic diseases. *Ann. Rheum. Dis.* **61** (Suppl. 2), ii96–ii99 (2002).
30. R. Haubner, F. Bruchertseifer, M. Bock, H. Kessler, M. Schwaiger, H. J. Wester, Synthesis and biological evaluation of a ^{99m}Tc-labelled cyclic RGD peptide for imaging the αvβ3 expression. *Nuklearmedizin* **43**, 26–32 (2004).
31. E. S. Mittra, M. L. Goris, A. H. Iagaru, A. Kardan, L. Burton, R. Berganos, E. Chang, S. Liu, B. Shen, F. T. Chin, X. Chen, S. S. Gambhir, Pilot pharmacokinetic and dosimetric studies of ^{18}F-FPPRGD2: A PET radiopharmaceutical agent for imaging $\alpha_v\beta_3$ integrin levels. *Radiology* **260**, 182–191 (2011).
32. M. Berman, E. Hoff, M. Barandes, D. B. Becker, M. Sonenberg, R. Benua, D. A. Koutras, Iodine kinetics in man—A model. *J. Clin. Endocrinol. Metab.* **28**, 1–14 (1968).
33. H. T. T. Phan, P. L. Jager, A. M. J. Paans, J. T. M. Plukker, M. G. G. Sturkenboom, W. J. Sluiter, B. H. R. Wolffenbuttel, R. A. J. O. Dierckx, T. P. Links, The diagnostic value of ^{124}I-PET in patients with differentiated thyroid cancer. *Eur. J. Nucl. Med. Mol. Imaging* **35**, 958–965 (2008).
34. P. B. Zanzonico, Age-dependent thyroid absorbed doses for radiobiologically significant radioisotopes of iodine. *Health Phys.* **78**, 60–67 (2000).
35. G. J. Kelloff, K. A. Krohn, S. M. Larson, R. Weissleder, D. A. Mankoff, J. M. Hoffman, J. M. Link, K. Z. Guyton, W. C. Eckelman, H. I. Scher, J. O'Shaughnessy, B. D. Cheson, C. C. Sigman, J. L. Tatum, G. Q. Mills, D. C. Sullivan, J. Woodcock, The progress and promise of molecular imaging probes in oncologic drug development. *Clin. Cancer Res.* **11**, 7967–7985 (2005).
36. M. R. Farnoud, N. Veirana, P. Derome, F. Peillon, J. Y. Li, Adenomatous transformation of the human anterior pituitary is associated with alterations in integrin expression. *Int. J. Cancer* **67**, 45–53 (1996).
37. J. V. Bonventre, Molecular response to cytotoxic injury: Role of inflammation, MAP kinases, and endoplasmic reticulum stress response. *Semin. Nephrol.* **23**, 439–448 (2003).
38. P. Kubes, The complexities of leukocyte recruitment. *Semin. Immunol.* **14**, 65–72 (2002).
39. R. Haubner, W. A. Weber, A. J. Beer, E. Vabuliene, D. Reim, M. Sarbia, K. F. Becker, M. Goebel, R. Hein, H. J. Wester, H. Kessler, M. Schwaiger, Noninvasive visualization of the activated αvβ3 integrin in cancer patients by positron emission tomography and [^{18}F]galacto-RGD. *PLOS Med.* **2**, e70 (2005).
40. R. J. Hyndman, Y. Fan, Sample quantiles in statistical packages. *Am. Stat.* **50**, 361–365 (1996).
41. D. Sarkar, *Lattice: Multivariate Data Visualization with R* (Springer, New York, 2010).
42. G. H. Bogush, M. A. Tracy, C. F. Zukoski IV, Preparation of monodisperse silica particles: Control of size and mass fraction. *J. Non-Cryst. Solids* **104**, 95–106 (1988).
43. E. Herz, A. Burns, D. Bonner, U. Wiesner, Large stokes-shift fluorescent silica nanoparticles with enhanced emission over free dye for single excitation multiplexing. *Macromol. Rapid Commun.* **30**, 1907–1910 (2009).
44. S. Sadasivan, A. K. Dubey, Y. Li, D. H. Rasmussen, Alcoholic solvent effect on silica synthesis—NMR and DLS investigation. *J. Sol-Gel Sci. Technol.* **12**, 5–14 (1998).
45. H. Ow, D. R. Larson, M. Srivastava, B. A. Baird, W. W. Webb, U. Wiesner, Bright and stable core-shell fluorescent silica nanoparticles. *Nano Lett.* **5**, 113–117 (2005).
46. R. Loevinger, T. Budinger, E. E. Watson, *MIRD Primer for Absorbed Dose Calculations* (Society of Nuclear Medicine, New York, 1991).

Acknowledgments: We thank H. Ow for supplying fluorescent silica particles, S. Patel for clinical trial design assistance, H. Hricak for technical input, and A. Burns for discussions and graphics support. **Funding:** This study was supported by the Laurent and Alberta Gershel PET Imaging Center of MSKCC. M.S.B. acknowledges support from a Research and Development award. Technical and radiochemistry services were provided by the MSKCC Radiochemistry-Cyclotron Core, supported in part by the NIH (P30-CA08748). Clinical trials services were provided by the Office of Clinical Research Staff. **Author contributions:** All authors have contributed as follows: prepared specimens (E.P., O.P.-M., Y.Y., and P.B.Z.), protocol development (M.S.B., R.D.C., S.M.L., and H.W.S.), conducting portions of the study (M.S.B., E.P., P.M., Y.Y., and H.S.), and data collection (E.P., O.P.-M., Y.Y., P.M., J.H., and H.K.); data analysis (M.S.B., P.B.Z., R.D.C., U.W., O.P.-M., E.P., Y.Y., P.M., H.W.S., H.K., J.H., S.M.L., and M.G.); and preparing the manuscript (M.S.B., U.W., and P.B.Z.). All authors discussed the results and implications and commented on the manuscript. **Competing interests:** U.W. is co-inventor of patents held by Cornell University on composition of matter of C dots. M.S.B., U.W., and S.M.L. are co-founders of a start-up company that has licensed the C dot patents and is currently raising funds to commercialize C dot technology. Pending patent for M.S.B. and MSKCC: "Multimodal silica-based nanoparticles" (PCT/US 4104-006-CIP-P-PCT/Intl: PCT/US14/30401). The authors declare that their spouses, partners, or children have no financial relationships relevant to the submitted work. Inquiries should be directed to the corresponding author. **Data and materials availability:** NIH Clinical Trials Registry (identifier number NCT01266096). Inquiries should be directed to the corresponding authors.

Submitted 13 May 2014
Accepted 4 September 2014
Published 29 October 2014
10.1126/scitranslmed.3009524

Citation: E. Phillips, O. Penate-Medina, P. B. Zanzonico, R. D. Carvajal, P. Mohan, Y. Ye, J. Humm, M. Gönen, H. Kalaigian, H. Schöder, H. W. Strauss, S. M. Larson, U. Wiesner, M. S. Bradbury, Clinical translation of an ultrasmall inorganic optical-PET imaging nanoparticle probe. *Sci. Transl. Med.* **6**, 260ra149 (2014).